

Research Article

A Numerical Model for Rock Cutting with Diamond Circular Saw Blade Based on Smoothed Particle Galerkin Method

Yongjun Tian , Yicun Sang , and Jie Liu 

Innovation College, Tianjin University of Technology and Education, Tianjin 300222, China

Correspondence should be addressed to Yongjun Tian; mywoner@126.com

Received 28 July 2022; Revised 9 November 2022; Accepted 30 November 2022; Published 15 December 2022

Academic Editor: Yu-Ling He

Copyright © 2022 Yongjun Tian et al. This is an open access article distributed under the Creative Commons Attribution License, which permits unrestricted use, distribution, and reproduction in any medium, provided the original work is properly cited.

A simulation approach was utilized to investigate the mechanics of cutting rock using the diamond circular saw blade in this paper. The smoothed particle Galerkin (SPG) method was used to numerically simulate three factors, including the dynamic mechanical behavior of the circular saw blade, the damage law of the circular saw blade, and the cutting force of the saw blade. The experimental comparison indicated that the SPG approach is feasible and accurate in the analysis and simulation of the rock cutting mechanism. The rock cutting is a process of material cyclic removal. The wear parts of the saw blade are most obviously manifested at the end of the saw segments. The water groove is also readily damaged in the alternating action, which has a significant impact on the service life of the saw blade. The effects of speed, cutting depth, and feed speed on the cutting force are discussed. The results reveal that these mentioned factors are important to the quality of rock cutting.

1. Introduction

The diamond circular saw blade is widely used in cutting and processing natural stones, which is an important industrial processing tool. The mechanical processing mechanism of rock differs from that of metal materials, and the stone cutting process is more sophisticated owing to the impact of the rock's brittleness [1]. The rock cutting process involves a wealth of the cutting mechanism, including rock fragmentation, crack generation, and material removal mechanism, as well as the nonlinear vibration response of the saw blade, stress distribution, dynamic cutting force, and the wear state of saw segments. As a result, predicting and analyzing the nonlinear structural response of the rock cutting process and its failure mode are critical for revealing the rock fracture mechanism, as well as playing an important role in the structural design of cutting tools. The dynamic response of rock cutting process encompasses a wide range of disciplines, including dynamics, mechanics, and acoustics. However, the damage, deformation, strain, and stress of the rock are difficult to acquire using experimental or theoretical models. CAE techniques provide a powerful means of explaining the damage, fracture, and fracture

behavior of the brittle and hard rock under high-speed impact and penetration. With the fast development of CAE technology [2], many three-dimensional numerical models have been developed for the study of the rock cutting process [3].

A Nonlinear Finite Element Method (FEM), which combines damage constitutive and erosion failure, was employed in Ref. [4] to study the rock cutting process. Wicaksana et al. examined the optimal rock cutting condition of disc cutters using the FEM-based ANSYS and AUTODYN models [4, 5]. With the creation of a three-dimensional rock cutting numerical model, the cutting performance of cutters by FEM for granitic rock was studied [6]. Gao et al. examined the rock cutting process considering the damage theory using FEM-based software [7]. The research finds normal load act was the most important component while cutting rock mass. The FEM-based commercial software such as LS-DYNA, ANSYS, Nastran, and ABAQUS has been extensively employed in the simulation process of rock cutting systems [4–7]. A variety of situations have proved the usefulness of numerical analysis as an option for the prediction of rock cutting performance. However, based on the following factors, the predictability

and accuracy of the three-dimensional finite element dynamic model may need to be improved:

- (1) Rock fragmentation, material separation, and saw kerf extension are all considerably different from the traditional FEM compared to reality. When finite element analysis is used to forecast rock damage and failure, the finite element mesh may become distorted and the calculation may be interrupted. As a result, a reasonably effective element removal method must be developed. The ERSION failure technique is used to prevent negative values of the Jacobian matrix determinant caused by finite element mesh deformation. When the solid elements reach the failure requirements, the deformed mesh is eliminated, but it creates an artificial vacuum in material physics, resulting in unstable values. Although the mesh rescaling strategy could mitigate the problem of negative volume, repetitive mesh rescaling tends to generate cumulative errors.
- (2) It does not preserve the mass and energy of the FEM cutting system in physics owing to the loss of a part of the mass and energy from the deleted element [8].
- (3) The erosion criteria in CAE software are based on the size of the element mesh, rock material model, and so on and are often determined by trial-and-error, resulting in a lack of predictability, reliability, and convenience [9].

Smoothed particle hydrodynamics (SPH) is a commonly used approach that does not depend on finite element grids [10]. The meshless method based on the Lagrange particle concept discretizes the computational domain into particles of fixed mass. It does not require element meshing or reconstruction techniques and it is suitable for analyzing material deformation and fracture damage under high pressure and high kinetic energy impact. It has been used in the simulation of bullet penetration into ceramic target plates and glass impact fragmentation. However, the meshless approach requires modifications according to the following considerations:

- (1) Although the SPH method is more accurate in describing large deformation problems than the FEM method, it needs to search for the mechanical information of the target particle and its surrounding particles at all times in the numerical calculation thereof. Thus, the calculation process of the SPH method is more complicated than that of FEM [11].
- (2) When dealing with the large deformation of materials, the SPH approach does not affect the space of the influence domain [8] and the size of the influence domain does not vary with material deformation. In the event of material stress, this approach can probably induce material fracture in numerical simulation, instability in the numerical calculation, and loss in computational accuracy.

To ease the aforementioned SPH situations, the stabilized conforming nodal integration (SCNI) algorithm

was raised by Chen et al. to improve the situation of the low-energy modes in the direct nodal integration (DNI) scheme [12, 13]. To improve the integration accuracy, the arbitrary-order Galerkin exactness for the SCNI method was presented under the framework of variational consistency in Ref. [14]. However, it is difficult to construct the conforming integration cells in fracture failure analysis due to the formation of a new interface. Thus, the SCNI technique was simplified to the stabilized nonconforming nodal integration (SNNI) method [15], which can be used to solve the problems of severe deformation with the variation of material damage. It has improved the SNNI scheme in Ref. [16], which provides greater simplicity for domain integration in material failure and separation analysis. Despite their effectiveness in impact and collision problems, the SCNI/SNNI integrated mesh-free approaches have low numerical accuracy and numerical diffusion.

To alleviate the situation, Wu et al. introduced the smoothed particle Galerkin approach [17], which is a meshless method based on a smoothed displacement field inside the Galerkin variational framework. The weak form of SPG formulation is integrated using the DNI algorithm to enhance computational efficiency [18]. A strain operator is used in the SPG formulation to stabilize the DNI technology. By changing the impact domain of the node and continuously updating the influence points surrounding the node, the SPG method tackles the problems of numerical fracture and distortion of the influence domain. Compared with FEM and SPH, the SPG method can not only obtain stable numerical results but also ensure that the time step of explicit analysis does not decrease obviously in the whole process. The SPG algorithm has been employed in impact and cutting processing [19], such as the extreme thread forming in the flow drill screw driving process and the penetration of bullets impacting the target plate. The characteristics of rock cutting processes include high stresses and enormous strain rates, substantial damage and separation of hard and brittle materials, complicated boundary conditions, and high frequency stress waves. These characteristics set obstacles to calculating the dynamic properties of hard and brittle materials via simulation. Therefore, several factors were not studied well, such as the material removal mechanism, rock fragmentation, and fracture of brittle materials during high-speed cutting of the diamond circular saw blade. The smoothed particle Galerkin (SPG) method is utilized in this paper to quantitatively examine the cutting reaction and damage distribution of hard brittle rock. Meanwhile, an adaptive anisotropic Lagrangian kernel is employed in the mesh-free approximation to deal with massive deformations, dynamic response, and contact-impact problems. A strain-based bond failure mechanism is presented to allow material damage and separation while avoiding numerical oscillation and artificial factors in the numerical failure analysis of the rock cutting process. The simulation results confirmed the effectiveness of the mesh-free approach SPG in high-speed rock cutting analysis.

2. Numerical Modeling

2.1. The Smoothed Particle Galerkin Method. The SPG method was developed for modeling material separation and failure under large deformation. SPG is a residual-based Galerkin element-free method. The SPG weak form is integrated using the direct nodal integration (DNI) technique [17].

Generally, the explicit dynamic formulation is given as follows:

$$M^{\text{lump}} \ddot{\mathbf{U}} = F^{\text{ext}} - F^{\text{int}}, \quad (1)$$

where M^{lump} is the lumped mass matrix; $\ddot{\mathbf{U}}$ is the vector of nodal accelerations; F^{ext} is the corresponding external force matrix; and F^{int} is the corresponding internal force matrix.

Using the DNI scheme to calculate F^{int} , it would produce low-energy modes. To improve the computational efficiency of the SPG method, the following approach may be applied. A strain operator derived from displacement smoothing theory is used to stabilize the DNI method.

The explicit dynamic version of the SPG formulation is given as follows:

$$M^{\text{lump}} \ddot{\mathbf{U}} = F^{\text{ext}} - F^{\text{int}} - F^{\text{stb}}, \quad (2)$$

where

$$F_i^{\text{stb}DNI} = \sum_{N=1}^{NP} B_i^T(X_N) \sigma(X_N) J^0 V_N^0, \quad (3)$$

where F_i^{stb} is the stabilization force which is derived from smooth displacement, B is the displacement smooth gradient matrix which contains the strain gradient, σ is the stabilization stress, and V_N^0 is an initial nodal volume of the node N .

2.2. The Bond-Based Failure Model. A discontinuity in the displacement field is considered in SPG [18] to model the material separation and failure in three-dimensional cutting or impacting analysis for hard and brittle materials. In this method, preventing numerical breakdown or numerical artifact is also considered. A strain-based bond failure mechanism is used in the numerical treatment. Each meshless particle in the SPG method has its own domain of influence [19], and the connection between particles in the domain is considered a connection bond. The bond resembles a chemical molecular bond [19]. The bond-based failure mechanism in material cutting or impacting analysis considers two neighboring particles that become disconnected whenever their averaged relative stretching and effective plastic strain reach their set values, respectively, which results in material fracture. Accordingly, the three-dimensional ellipsoidal cubic kernel function for neighbor particles, i.e., M and N , can be defined as follows:

$$\phi_M^a(X_N) = \begin{cases} 0 & e_{MN} > e_{\text{crit}} \text{ and } \varepsilon_{MN}^P > \varepsilon_{\text{crit}}^P, \\ \phi_1\left(\frac{X_M}{h_1^n}\right) \phi_1\left(\frac{Y_M}{h_2^n}\right) \phi_1\left(\frac{Z_M}{h_3^n}\right) & \text{otherwise,} \end{cases} \quad (4)$$

where

$$\varepsilon_{MN}^P = \frac{\sum_{\text{eff}}^P(X_M) + \sum_{\text{eff}}^P(X_N)}{2}, \quad (5)$$

$$e_{MN} = \frac{\|x_M - x_N\|}{\|X_M - X_N\|},$$

where ε_{MN}^P is the averaged effective plastic strain at particle M and particle N ; ε_{MN}^P is the relative stretch between nodes M and N ; $\varepsilon_{\text{crit}}^P$ is critical effective plastic strain; $\|x_M - x_N\|$ is the length of the bond for neighbor particles M and N during the initial period; a is the support size in the kernel function; and e_{crit} is critical relative stretch.

The bond-based failure mechanism is depicted in Figure 1. Each particle in SPG has a certain influence domain. The supports of the neighbor particles M and N are represented by the two large circles separately. Seven bonds are connected to particle M in the initial configuration, i.e., bonds M-N, M-I, K-L, K-J, K-Q, K-T, and K-P. Six bonds are connected to particle N . The bond M-N between a pair of particles M and N is disconnected or broken whenever reaches their failure criteria, i.e., $e_{MN} > e_{\text{crit}}$ and $\varepsilon_{MN}^P > \varepsilon_{\text{crit}}^P$, that is, $\phi_M^a(X_N) = 0$ and $\phi_N^a(X_M) = 0$. Therefore, the shape function of particle M is set to zero at particle N , which causes material failure, as shown in Figure 1(b). However, $\phi_M^a(X_I) \neq 0$ and $\phi_N^a(X_E) \neq 0$, which means the rest bonds except bond M-N are valid. This indicates that the state variables at nodes M and N will still evolve regularly according to the deformation and material law. The only change is that their contiguous particles have one less node. As a result, the criterion for destructive separation of the material is determined by the connection between the particles. This differs from the FEM failure mechanism, which eliminates the elements directly (loss of mass) and physically violates the energy conservation equation (loss of momentum). It is shown that the bond-based failure mechanism guarantees mass and momentum, achieving energy conservation.

3. Establishing a Numerical Model

The cutting process of rock is modeled by the SPG method and compared with the experimental test data. Convergence and sensitivity studies were performed on the main SPG parameters to check the stability and reliability of the nonlinear analysis in the rock cutting process.

3.1. Geometry Conditions and Boundaries. The diamond circular saw blade and the cuboid rock are modeled, as shown in Figure 2. The diameter of the diamond circular saw blade was 350 mm. The diameter of the chuck was 120 mm. The thickness of the saw blade substrate was 2 mm, and the thickness of the diamond segment was 3 mm. To improve the computational efficiency, only the vicinity of the contact areas in the workpiece (the cuboid workpiece that may be undergoing severe deformation) was divided into the SPG system, whereas other parts with less deformation occurred in the remaining majority including the rest of the

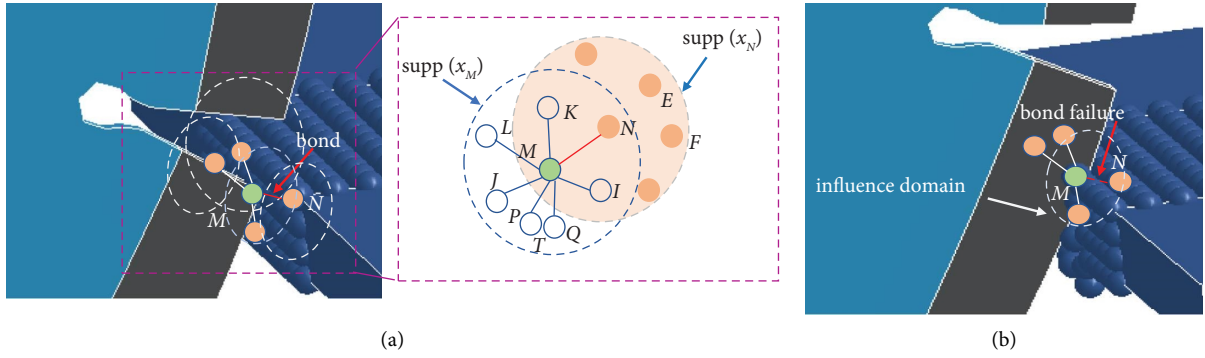


FIGURE 1: Illustration of SPG bond failure mechanism: (a) forming of the SPG bond; (b) breaking of the SPG bond.

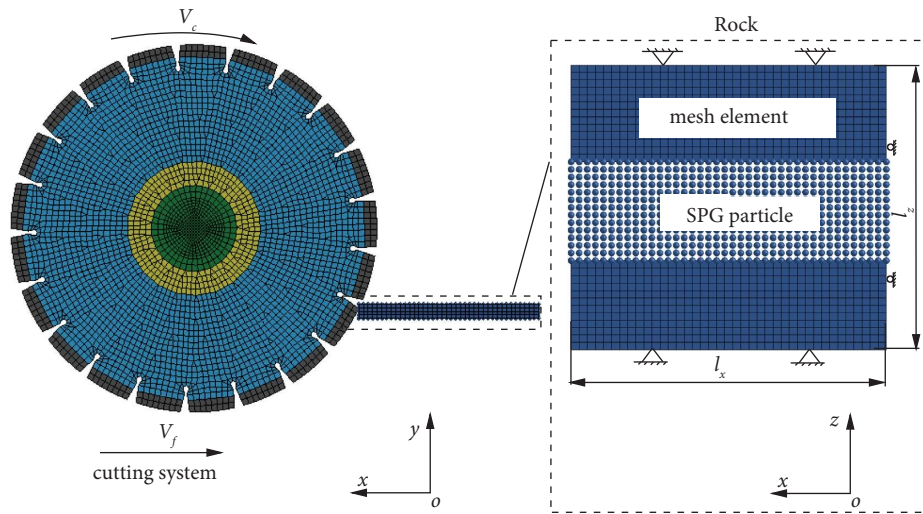


FIGURE 2: The diamond circular saw blade-rock cutting model.

workpiece, collar, spindle, and circular saw blade which were modeled by the FEM formulation. In addition, the cuboid workpiece, which may be undergoing severe deformation, was modeled with a length of 170 mm, a width of 32 mm, and a height of 10 mm, as shown in Figure 2. Specifically, the feasibility of coupling FEM with SPG has proven effective [13, 17].

The SPG analysis begins with the classical FEM. The 3D FE meshes can be converted into SPG forms using the *SECTION_SOLID_SPG in LS-DYNA commands. It should be noted that for the SPG analysis, "FORM" on the *SECTION_SOLID_SPG should be set to 47. "KERNEL" on the present keyword should be set to Semipseudo Lagrangian kernel. The crucial relative stretch is 1.005 unless otherwise indicated, and the normalized support size of 1.5 is utilized for the SPG kernel function in X, Y, and Z direction. It should be noted that for the coupled FEM-SPG simulation, the wave can pass nicely through the interface from the FEM zone to the SPG zone (or through the SPG region to the FEM region), with no significant reflection observed at the FEM-SPG interface [18]. As a result, in the rock cutting model, the coupled FEM-SPG discretization can be used to simulate a dynamic event.

The boundary conditions of the cutting system were the following: (a) both the left surface and right surface element groups of the workpiece were constrained in the y -direction; (b) the bottom element group of the cuboid except for SPG particles was constrained at six degrees of freedom (6 DOF); (c) the back surface of the workpiece was constrained in the x -direction; and (d) the *NON-REFLECTING BOUNDARY was adopted in the abovementioned area except for the front to eliminate the influence of strain and stress wave reflection on rock fracture and damage. The circular saw blade rotated around the z -axis at a constant peripheral speed $\omega = 230 \text{ rad/s}$ and traversed in the x -direction at a speed of $v_f = 10 \text{ mm/s}$.

The *AUTOMATIC_NODE_TO_SURFACE contact algorithm was applied between the segments of the saw blade and the workpiece in the cutting process. Meanwhile, the dynamic friction factor was set to 0.25 and the static friction factor was set to 0.20. The slave part is defined by the node set (SPG particles) in the present contact algorithm. The master parts are defined by the saw blade segments and the substrate. After the dynamic numerical model was structured and simulated, the following assumptions were made: (a) the wear of the segment is negligible during the process; (b) the cutting chips do not interact with the saw blade after

separating from the rock; (c) the rock is a homogeneous material without initial damage or fracture; and (d) no liquid coolant was used in the experiment. Therefore, dry surfaces are assumed in the numerical simulation.

3.2. Material Model. The deformation mechanism of granite is complex and its fracture mode is mainly brittle fracture, accompanied by compression and shear failure under high pressure. In the numerical simulation, the material constitutive model has a direct impact on the accuracy of the calculation consequences of the dynamic statistics of the cutting process.

The Karagozian and Case Concrete (KCC) model can accurately simulate the dynamic mechanical properties of brittle materials, describe the nonlinear behavior of materials subjected to dynamic impact loading, and reproduce the mechanical behavior of rocks and other fragile materials under high-speed impacts [20, 21]. Therefore, the KCC damage model is used to simulate the dynamic damage behavior of rock or concrete, which describes the strength development and damage evolution of hard and brittle materials based on three pressure-related shear failure surfaces, as shown in Figure 3.

The main characteristic of the yielding of rock materials is its dependence on the average pressure. The failure surfaces of rock materials are curved and have smooth meridians. As a result, the surfaces can be more conveniently described in the Haigh–Westergaard stress space. The following equation is the principal that stresses in the Haigh–Westergaard system:

$$\begin{bmatrix} \sigma_1 \\ \sigma_2 \\ \sigma_3 \end{bmatrix} = \frac{1}{\sqrt{3}} \begin{bmatrix} \xi \\ \xi \\ \xi \end{bmatrix} + \sqrt{\frac{2}{3}} \rho \begin{bmatrix} \cos \theta \\ \cos \left(\theta - \frac{2\pi}{3} \right) \\ \cos \left(\theta + \frac{2\pi}{3} \right) \end{bmatrix}, \quad (6)$$

where ρ , θ , and ξ are the Haigh–Westergaard coordinates, which can be expressed as follows:

$$\left. \begin{aligned} \xi &= \frac{1}{\sqrt{3}} I_1 = \sqrt{3} p \\ \rho &= \sqrt{2J_2} = \sqrt{\frac{2}{3}} \sigma_{\text{eq}} \\ \cos(3\theta) &= \left(\frac{r}{q} \right)^3 = \frac{3\sqrt{3}}{2} \frac{J_3}{J_2^{3/2}} \left[r = 3 \left(\frac{1}{2} J_3 \right)^{1/3} \right] \end{aligned} \right\}, \quad (7)$$

where I_1 is the first principal invariant of the Cauchy stress; J_2 is the second principal invariant of the deviatoric part of the Cauchy stress; J_3 is the third principal invariant of the deviatoric part of the Cauchy stress; p is the hydrostatic pressure; and σ_{eq} is the equivalent stress, which is equal to q .

The failure surface function of KCC $\Phi(\rho, \theta, \xi, \lambda)$ is described by the following in terms of the Haigh–Westergaard stress invariants:

$$\Phi(\rho, \theta, \xi, \lambda) = \sqrt{\frac{3}{2}} \rho - \varphi(\theta, \xi, \lambda), \quad (8)$$

where function $\varphi(\theta, \xi, \lambda)$ is the failure surface of the KCC model and λ is the damage parameter.

The function $\varphi(\theta, \xi, \lambda)$ is calculated using the linear interpolation functions with a pair of fixed-strength and independent-strength surfaces. These interpolation functions are different for softening and hardening. The function $\varphi(\theta, \xi, \lambda)$ can be described by the following equation:

$$\varphi(\theta, \xi, \lambda) = \begin{cases} r_f \frac{r(\theta)}{r_c} [\hat{\sigma}_y(p)]; & (\lambda \leq \lambda_0), \\ r_f \frac{r(\theta)}{r_c} \{ \eta(\lambda) [\hat{\sigma}_m(p) - \hat{\sigma}_y(p)] + \hat{\sigma}_y(p) \}; & (\lambda_0 \leq \lambda \leq \lambda_m), \\ r_f \frac{r(\theta)}{r_c} \{ \eta(\lambda) [\hat{\sigma}_m(p) - \hat{\sigma}_r(p)] + \hat{\sigma}_r(p) \}; & (\lambda_m \leq \lambda), \end{cases} \quad (9)$$

where λ_m and λ_0 correspond to the points at which the softening and hardening regimes start, respectively; the yield-maximum and maximum-residual strength surfaces are the pairs for hardening and softening, respectively; $\hat{\sigma}_y(p)$, $\hat{\sigma}_m(p)$, and $\hat{\sigma}_r(p)$ are shear failure surfaces, corresponding to the ultimate strength surface, yield strength surface, and

residual strength surface, respectively, when the Lode angle θ is equal to 60° ; λ is the damage parameter of the interpolation damage function $\eta(\lambda)$; the term $\hat{\tau}[\Psi(p), \theta]$ (equal to $r(\theta)/r_c$) is the nondimensional function determined between radius parameter $r(\theta)$ and distance parameter r_c (see Figure 3(b)); and λ is damage parameter, which is

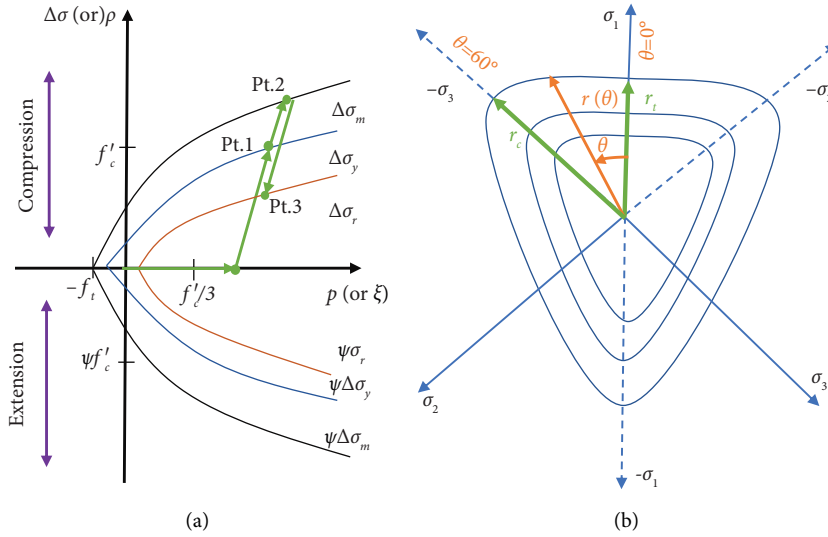


FIGURE 3: Failure surfaces of the KCC model in (a) compression/tension meridian; (b) deviatoric plane.

defined separately for compression and tension according to the following equation:

$$\lambda = \begin{cases} \int_0^{\bar{\varepsilon}^p} \frac{d\bar{\varepsilon}^p}{r_f(1+(p/r_f T)^{b_1})} p \geq 0, \\ \int_0^{\bar{\varepsilon}^p} \frac{d\bar{\varepsilon}^p}{r_f(1+(p/r_f T)^{b_2})} p < 0, \end{cases} \quad (10)$$

where b_1 is the compression damage coefficient, b_2 is the uniaxial tensile damage coefficient, r_f is the dynamic increase parameter, T is the tensile strength, and $\bar{\varepsilon}^p = \sqrt{(2/3)d\varepsilon_{ij}^p d\varepsilon_{ij}^p}$ is the effective plastic strain.

In equation (9), $r(\theta)$ is the current radius of the failure surface (see Figure 3(b)) which is computed using the following equation:

$$r(\theta) = \frac{2r_c(r_c^2 - r_t^2)\cos\theta + r_c(2r_t - r_c)\sqrt{4(r_c^2 - r_t^2)\cos^2\theta + 5r_t^2 - 4r_t r_c}}{4(r_c^2 - r_t^2)\cos^2\theta + (2r_t - r_c)^2}, \quad (11)$$

where r_c and r_t correspond to, respectively, the distance of the failure surface from the hydrostatic axis at the compressive meridian and the distance of the failure surface from the hydrostatic axis at the tensile meridian.

$\hat{r}[\Psi(p), \theta]$ is the shape of the failure criterion in the deviatoric plane. The function was originally derived from equation (11), which can be described as the following equation:

$$\hat{r}[\Psi(p), \theta] = \frac{2(1 - \Psi^2)\cos\theta + (2\Psi - 1)\sqrt{4(1 - \Psi^2)\cos^2\theta + 5\Psi^2 - 4\Psi}}{4(1 - \Psi^2)\cos^2\theta + (1 - 2\Psi)^2}, \quad (12)$$

where $\Psi(p)$ is a strength index and θ is the Lode angle, where r_c and r_t correspond to, respectively, the distance of the failure surface from the hydrostatic axis at the compressive meridian and the distance of the failure surface from the hydrostatic axis at the tensile meridian.

$\Psi(p)$ is a linear piecewise function on the full range of pressure, which is calculated by

$$\Psi(p) = \begin{cases} \frac{1}{2} (-f_t \leq p \leq 0) \\ \frac{1}{2} + \frac{3f_t}{(2f'_c)} \left(p = \frac{f'_c}{3} \right) \\ \frac{\alpha f'_c}{\alpha_0 + 2\alpha f'_c/3/\alpha_1 + 2\alpha_2 f'_c/3} \left(p = \frac{2\alpha f'_c}{3} \right) \\ 0.753 (p = 3f'_c) \\ 1.0 (p \geq 8.45f'_c) \end{cases}, \quad (13)$$

where f_t is the principal tensile strength, f'_c is the uniaxial compressive strength, α_1 , α_2 , and α_0 are the user-defined input parameters, and α is a parameter related to the compression test.

As shown in Figure 3(a), the KCC model has three independent failure surfaces in the compressive meridian, i.e., $\Delta\sigma_y$ is the yield strength surface, $\Delta\sigma_m$ is the maximum strength surface, and $\Delta\sigma_r$ is the residual strength surface, and the intensity surface functions are denoted as follows:

$$\begin{aligned} \Delta\sigma_m &= a_0 + \frac{p}{a_1 + a_2 p}, \\ \Delta\sigma_r &= \frac{p}{a_{1y} + a_{2y} p}, \\ \Delta\sigma_y &= \sigma_{0y} + \frac{p}{a_{1y} + a_{2y} p}, \end{aligned} \quad (14)$$

where $\Delta\sigma_y$ controls the initiation of plastic deformation of the rock, $\Delta\sigma_m$ is dependent on loading conditions, and $\Delta\sigma_r$ determines the post-failure stiffness of the material. The state of stress is determined by linear interpolation between $\Delta\sigma_y$, $\Delta\sigma_m$, and $\Delta\sigma_r$ surfaces, as shown in Figure 3. The response of the rock material to the initial loading is modeled as a linearly elastic deformation before reaching $\Delta\sigma_y$ surface. A hardening plasticity response occurs after yielding and before reaching the $\Delta\sigma_m$ surface. A softening response occurs after reaching the maximum strength and before reaching the $\Delta\sigma_r$ surface.

The KCC model must be combined with an equation of state (EOS) to describe the volumetric response of the concrete or rock material. The Tabulated Compaction model is used as EOS in the KCC model [22, 23], which is based on a piecewise nonlinear relationship between pressure p and volumetric strain V . The form of the EOS is given by

$$p = C(\varepsilon_V) + \gamma H(\varepsilon_V)E, \quad (15)$$

where ε_V is volumetric strain; $C(\varepsilon_V)$ is the volumetric pressure value corresponding to ε_V ; H is an additional unitless tabulated function; and E is initial internal energy.

The main material parameters of the rock are plotted in Table 1.

PR is Poisson's ratio; UCF and RSIZE are unit conversion factors; NOUT is the output selector for effective plastic strain; A0 is unconfined compressive strength; A1 and A2 are the maximum shear failure surface parameters, respectively; and NPTS is the number of points in versus damage relation.

3.3. Theoretical Study of the Cutting Force. The cutting force is an important parameter to consider during the cutting process. It may not only fully reflect the mechanism and tool wear of the cutting process, but it can also have a direct impact on saw blade life and cutting efficiency. The cutting force of the tool in the process of cutting hard and brittle rock with diamond saw blade is complex, as shown in Figure 4, due to the normal force, tangential force, and axial force composition.

The normal force F_n is attributable to the impact of the cutting tool on the rock and the tangential force F_t is the friction between the workpiece and the tool. The normal tangential forces are not easily obtained, but horizontal and vertical forces are relatively easy to obtain in the cutting process.

The formula for the cutting force is as follows:

$$F = \sqrt{F_x^2 + F_y^2} = \sqrt{F_n^2 + F_t^2}. \quad (16)$$

The relationship of cutting forces is shown in Figure 4, which can be expressed as follows:

$$\begin{aligned} \beta &= \cos^{-1} \left(1 - \frac{2a_p}{d} \right), \\ \delta &= \tan^{-1} \left(\frac{F_x}{F_y} \right), \end{aligned} \quad (17)$$

where d is the saw blade diameter.

The force F_n and force F_t in Figure 4 can be indicated as follows:

$$\begin{aligned} F_t &= F \sin(\alpha - \delta) = F_x \sin \alpha - F_y \cos \alpha, \\ F_n &= F \cos(\alpha - \delta) = F_x \cos \alpha - F_y \sin \alpha, \\ \alpha &= \varepsilon + \delta = k\beta, \\ k &= \frac{\varepsilon + \delta}{\beta}, \end{aligned} \quad (18)$$

where k is determined by the contact position between workpiece and cutting tool.

The saw segments being cut are subjected to the corresponding tangential and normal forces, with the force

TABLE 1: The main parameters of KCC provided for the full input mode.

Density (ton/mm ³)	PR	A0 (MPa)	NOUT	A1
2.77E-9	0.20	40.2	2.0	0.4463
A2 (MPa ⁻¹)	UFC (psi/MPa)	RSize (in/mm)	NPTS	
5.282E-4	145.0	0.03937	13.0	

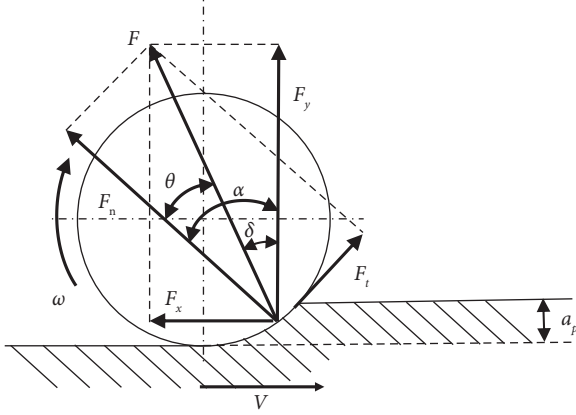


FIGURE 4: The model for cutting system. F : cutting force, V : feed speed, ω : rotation speed, F_x : horizontal force, F_y : vertical force, F_t : tangential force, F_n : normal force, F_t : tangential force, and a_p : cutting depth.

locations being the top and sides of the segments, and the area of each segment is A_n and A_t , separately. The uniform load on a single side is $P_t = F_t / (A_t/2)$, and the uniform load on the top surface of a single tooth is $P_n = F_n / (A_n/2)$, showing that there is a concentrated load around the saw teeth during the sawing process.

4. Numerical Results and Discussion

4.1. Calibration and Verification. Generally, when the diamond circular saw blade rotates at high speeds, it causes lateral vibration, which can accelerate cutting tool wear and failure. Moreover, increasing lateral vibration has a negative impact on machining quality and cutting efficiency. Furthermore, increased transverse vibration might enhance the cutting noise. As a result, the lateral vibration velocity of the saw blade is a key parameter of the cutting simulation. To verify the simulation algorithm's dependability, the OFV505 laser noncontact vibration measurement device is utilized to obtain lateral vibration data from measuring locations on the saw blade during processing. The measurement positions were chosen to be 70 mm (0.4 R) and 140 mm (0.8 R) from the rotating shaft's center, as illustrated in Figure 5. The lateral vibration responses of the test spots were derived by simulations using the SPG and the FEM, respectively, and the experimental results are displayed in Figure 6.

The results are as follows:

- (1) Because the rock is a nonhomogeneous material with hard spots, the saw blade's lateral vibration speed might vary dramatically throughout the cutting process.

- (2) The small transverse vibration amplitude in the numerical calculation is due to the simulation process, which defines the stone as a material with uniform texture and does not take into account the feedback effect of other saw machine structures and external interference factors in the actual cutting process.

- (3) The difference between the finite element calculation results and the experimental findings is significant, with an error of 10% to 25% caused by mesh distortion during the calculation process. The mesh failure technique is used to avoid the phenomenon of negative determinant values of the accord ratio matrix caused by element distortion. In another words, when the workpiece elements reach the failure criterion, they will be deleted directly, causing artificial vacancies in the material and resulting in the loss of momentum and mass. There was significant agreement between the SPG estimated values and test results, with errors between 5% and 11%, indicating that the SPG method is more suitable for stone cutting process simulation.

- (4) The vibration response of the saw blade becomes more focused and noticeable as one moves away from the central hole. After being subjected to discontinuous alternate pressures, the segments vibrate violently during the cutting process, causing the substrate surrounding them to vibrate continuously. However, the closer to the center of the saw blade, the more obvious the action of the saw blade clamping disc on the saw blade, so the better the stability of the structure, the lower the vibration speed.

4.2. SPG Parameter Sensitivity. The cutting forces were calculated using the boundary conditions described in Section 3.2. Table 2 shows the results of the finite element analysis for the bond fracture criteria with varied parameters. When the effective plastic strain for element erosion was reduced from 0.4 to 0.2, the difference between the numerical and experimental results increased from 18.4% to 28.7%, indicating that the FEM solutions are clearly dependent on the failure criterion and are not similar to the SPG solutions.

The variation regularities of the average lateral vibration velocity of the circular saw blade with varied SPG parameters are plotted in Tables 3 and 4. It is illustrated in Table 3 that the SPG simulation is not sensitive to the different bond fracture criteria (effective plastic strain): $\epsilon_{crit}^p = 0.05$, $\epsilon_{crit}^p = 0.2$, $\epsilon_{crit}^p = 0.4$, $\epsilon_{crit}^p = 1.6$, and $\epsilon_{crit}^p = 1.98$. The differences among the numerical solutions were marginal, and the

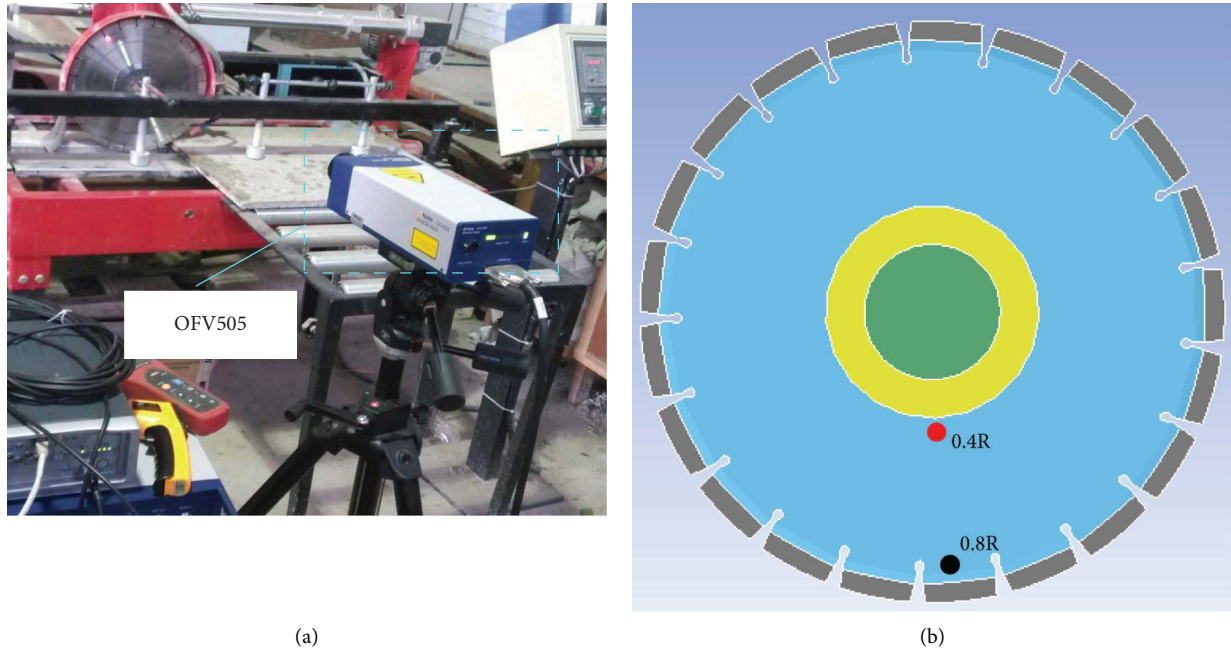


FIGURE 5: Vibration speed measurement: (a) laser vibrometer OFV505; (b) measurement points.

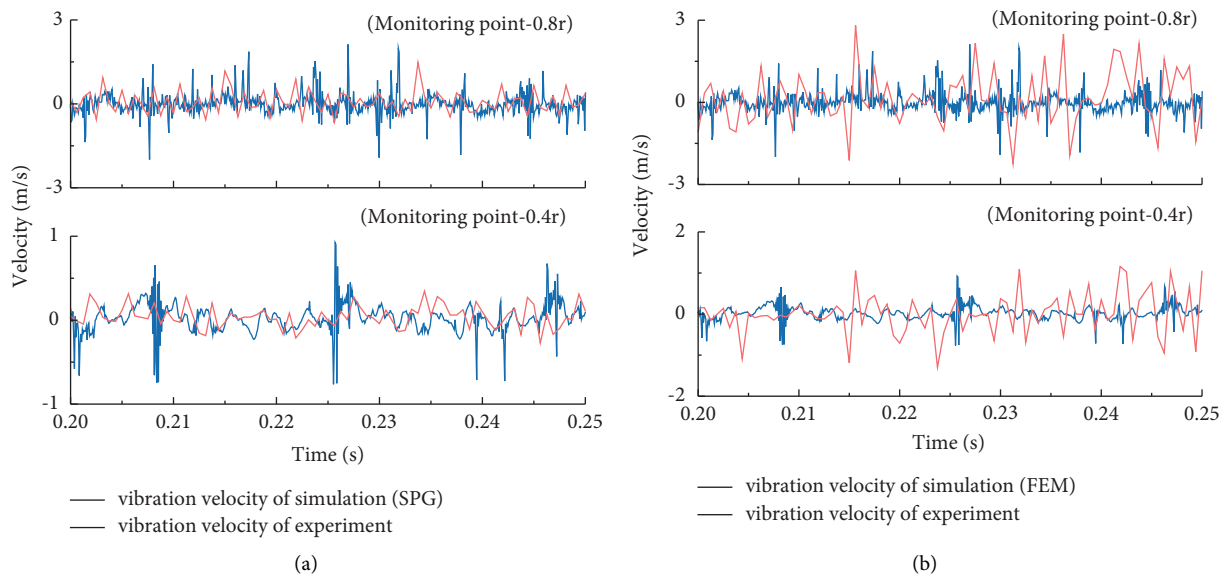


FIGURE 6: The lateral vibration speed of saw blade: (a) the vibration velocity of SPG simulation and experiment; (b) the vibration velocity of FEM simulation and experiment.

maximum error with the experimental value is controlled within 10%. Although there are significant differences in the failure criterion, which is notably different from FEM using the erosion technique, the numerical answers derived using the SPG method are still probably close. This insensitivity to bond failure criteria might be the problem that is driven by momentum [17], which mitigates the solution dependence on material strength. Table 4 displays the lateral vibration velocity obtained with three different normalized SPG support sizes with the same values in the X, Y, and Z directions: 1.4, 1.5, 1.6, 1.7, and 1.8, respectively. The

sensitivity to the normalized SPG support size is negligible, and the maximum error with the experimental value is controlled within 6%.

Compared with the FEM, the SPG algorithm has the following advantages in simulating the rock cutting process: (1) Modeling is simple. There is no need to discretize the large deformation region into fine finite element meshes and add the element failure keyword. If the calculation model is more complicated, the SPG approach has more visible advantages in modeling; to enhance the computation performance, only the large deformation region needs to be

TABLE 2: Comparison of FEM simulation results and experimental results.

Effective plastic strains	Simulation velocity (m/s)	Experiment velocity (m/s)	Errors (%)
0.2	1.03	0.87	18.4
0.4	1.12	0.87	28.7

TABLE 3: Comparison of SPG simulation with different effective plastic strain values and experimental results.

Effective plastic strains	Simulation velocity (m/s)	Experiment velocity (m/s)	Errors (%)
0.05	0.81	0.87	6.89
0.20	0.93	0.87	-6.89
0.40	0.91	0.87	-4.59
1.60	0.89	0.87	-2.29
1.98	0.95	0.87	-9.19

TABLE 4: Comparison of SPG simulation results with different support sizes and experimental results.

Support sizes	Simulation velocity (m/s)	Experiment velocity (m/s)	Errors (%)
0.05	0.85	0.87	-2.29
0.20	0.88	0.87	-1.14
0.40	0.91	0.87	-4.59
1.60	0.92	0.87	-5.74
1.98	0.89	0.87	-2.29

discretized into SPG particles; (2) The calculation is highly accurate. The SPG approach can more correctly explain physical phenomena such as rock material separation and the splash process of rock chips under high-speed impact; (3) It has good adaptability. The SPG approach can adapt to a dynamic environment with little reliance on element (particle) density, failure criterion, kernel update frequency, and support size.

4.3. The Cutting Process between the Circular Saw Blade and the Rock. The simulation model was dynamically analyzed to study the rock damage and damage patterns in different periods, including the dynamic damage of the diamond circular saw blade. The numerical simulation results of the cutting process, including the distribution of the von Mises stress of each part, are shown in Figures 7 and 8.

The von Mises stress is equivalent stress based on shear strain energy that uses stress contours to represent the stress distribution within the model, enabling the most dangerous areas of the model to be quickly identified. Obviously, the higher the stress value is, the more vulnerable the region is to damage. The following formula is used to calculate the von Mises stress:

$$\sigma_s = \sqrt{\frac{1}{2} [(\sigma_1 - \sigma_2)^2 + (\sigma_2 - \sigma_3)^2 + (\sigma_3 - \sigma_1)^2]}, \quad (19)$$

where σ_1 , σ_2 , and σ_3 refer to the first principal stress, second principal stress, and third principal stresses, respectively.

4.3.1. The von Mises Stress of the Rock in the Cutting Process. As shown in Figure 7(a), at the initial stage of cutting, a concentrated force was exerted on the rock by the arc segments. As a result, some SPG particles in front of the blade segment were subjected to the combined action of impact pressure and shear stress in Figures 7(a)-I. The

particles were reserved and did not fail primarily due to elastic deformation, local plastic deformation, and compressive press. Thus, during sequential cutting, the zone in the contact area between the rock and saw blade causes further compression and shear deformation, and the displacement of the rock particles in the area changes to reach a new equilibrium in Figure 7(a)-II. As shown in Figure 7(a)-III, around the diamond saw segment, the SPG particles failure and separation in the contact region were clearly observed due to the compressive stress and shear stress, and a small quantity of SPG particles (fragments) was separated from the base rock. The rock was in the small-scale extrusion stage, and the crushed zone is expanded in Figure 7(b). As shown in Figure 7(c), the workpiece forms an obvious fracture area. The rock around the saw segments is subjected to the combined action of tensile stress and shear stress, which aggravates the damage. The internal material was damaged and broken, and debris chips were also observed. Meanwhile, with the distance of the saw blade cutting into the rock increasing, the initial saw kerf was formed. As shown in Figure 7(d), with increasing cutting distance, the damaged and broken regions of the rock expanded rapidly and a considerable number of chips were separated from the workpiece, at which point the cutting process was at the stage of large-scale fracture, gradually expanding to form an obvious saw kerf. With the rotating circular saw blade linearly feeding, the large-scale fracture of brittle rock occurs repeatedly. Therefore, it was concluded that brittle disintegration is the main spalling mode during damage and destruction of the material. Specifically, the compressive and shear stresses on the rock during cutting are the main cause of brittle damage to the rock, which is due to various defects and concentration stress in the rock that cause fracture damage and expansion under shear and compressive.

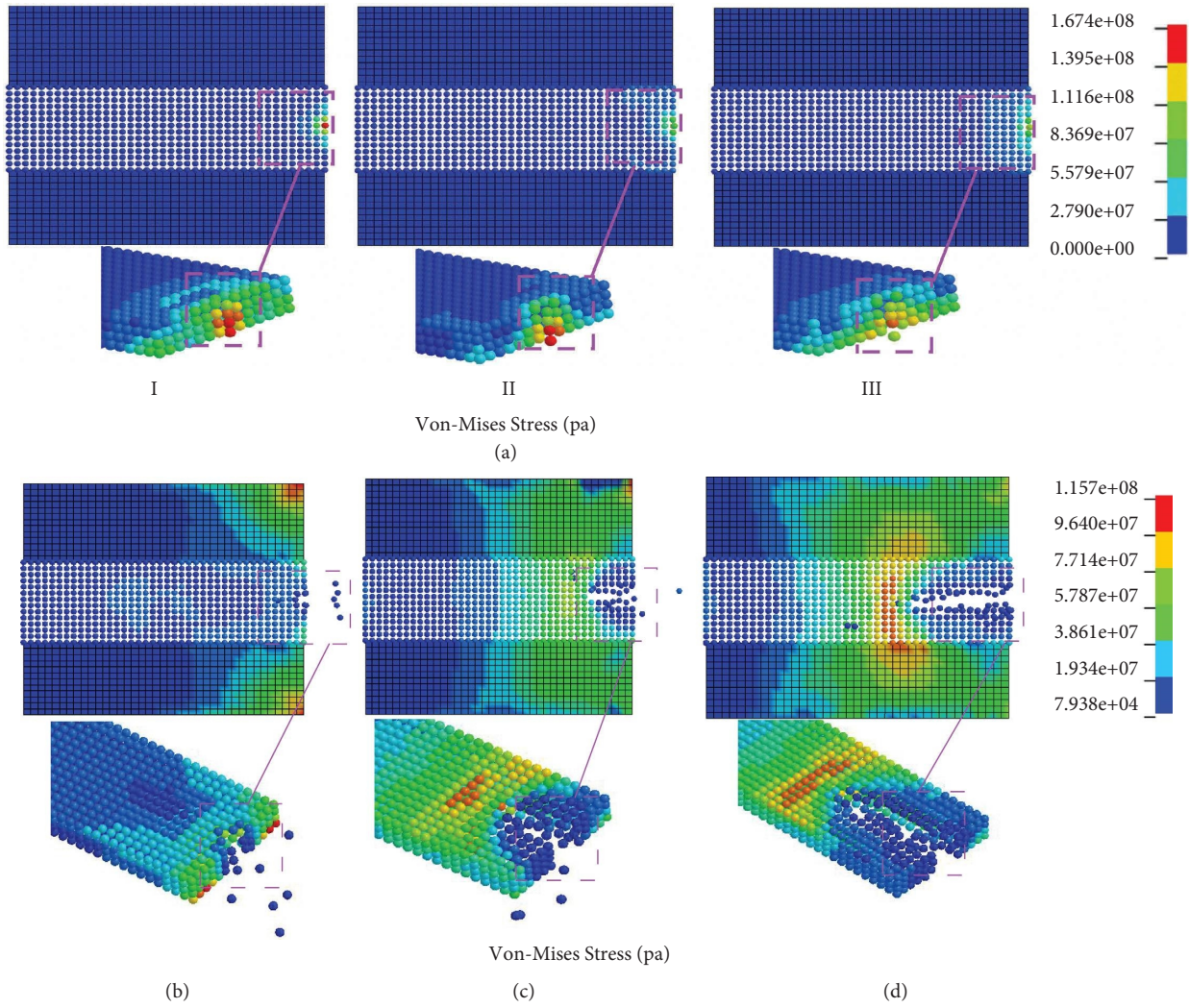


FIGURE 7: The cutting model simulation process based on SPG: (a) elastic deformation and local plastic deformation; (b) small-scale extrusion; (c) small-scale fracture; (d) large-scale fracture.

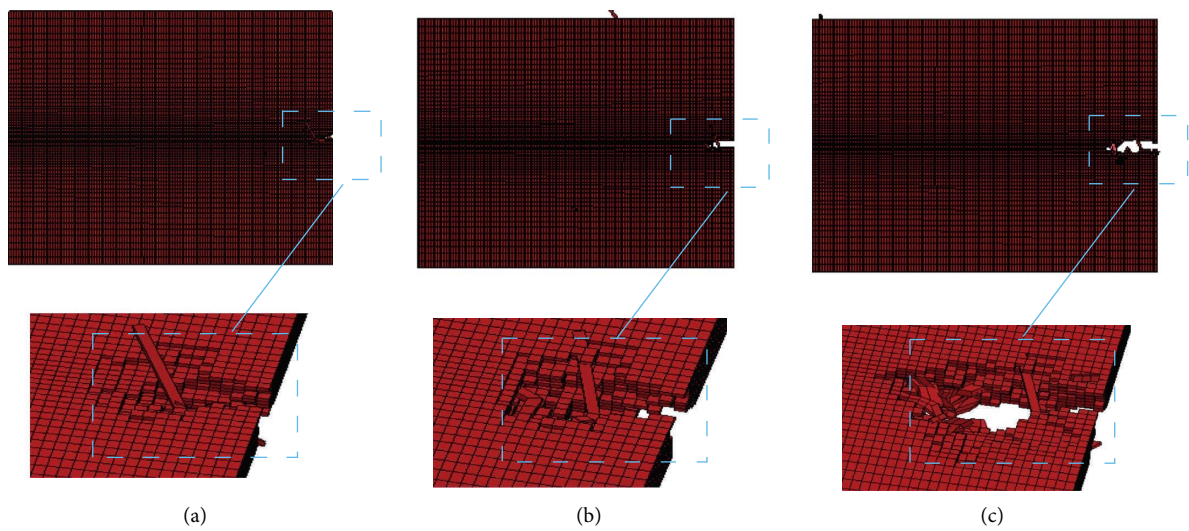


FIGURE 8: The cutting model simulation process based on FEM.

It is shown that the SPG model can simulate the dynamic damage process of rocks under the impact of diamond saw blade at high speed from a microscopic perspective. It is found that the process of the indentation of a cutting tool into the rock starts with the development of concentrated stress under the saw blade. Moreover, the damage process of rocks under the circular saw blade is a cycle of elastic deformation, local plastic deformation, small-scale extrusion, and large-scale fracture.

The high-speed rotating tool comes into contact with the workpiece during the cutting process, causing the rock to fail due to the high-speed impact, resulting in rock fragmentation and damage. To study the failure forms, the shear and pressure forces should be extracted. As shown in Figure 9, two test points were set up on the cutting path to investigate the failure mode of the cutting system. It should be noted that negative pressure means the press is tensile stress; positive press denotes compressive stress. For test particles in the damage zone, the tensile stress, compressive stress, and shear force versus time are shown in Figure 10. For test particle 1, the maximum shear force reached 12.26 MPa, and the maximum compressive force reached 13.4 MPa with particle splash. As a result, particle 1 is compressive failure. As shown in Figure 10(a), the compressive force of the particle 2 reached 2.25 MPa, while the shear force reached 4.21 MPa at 0.6 ms (Figure 10(b)) followed by the rock particle damage and separation, indicating that the rock is in shear failure. Therefore, the damage to the rock is a combination of one or more of shear damage, tensile damage, and compression damage in the cutting process.

In Figure 8, the rock fragments, material separation, and saw kerf extension during cutting are not obvious in the finite element model. The workpiece is prone to mesh distortion (negative volume) and other phenomena in the finite element method to simulate the rock cutting process. In addition, when the stress value in the contact region reaches a specific level, the deformed mesh may be deleted immediately, causing an artificial vacancy in the physical material, and the sudden decrease in pressure may generate an inaccuracy that is difficult to estimate. However, the SPG technique and cutting test results agree well, the saw kerfs are generally regular, and the width variance is between 3% and 10% relative to the experiment, as shown in Figure 11, with width deviations ranging from 9% to 26% compared to the experiment.

4.3.2. The von Mises Stress of the Circular Saw Blade in the Cutting Process. The easy-wear and first-wear components of the tool can be identified using the stress distribution law of the circular saw blade, which offers a foundation for design and processing. Figure 12 depicts the von Mises stress cloud diagram of the circular saw blade at multiple moments throughout the cutting process. It can be deduced that the stress concentration is most likely to occur during the cutting process at the front end of the saw tooth touching the rock. During the cutting process, the contact area between the saw blade and the stone is subjected to a combination of strong compression and friction, resulting in obvious local

stress concentration and a larger stress gradient, as well as evidence that the area was severely worn. The maximum stress of the saw tooth reaches 280 MPa at the front and bottom edges, and the von Mises stress in the circumferential direction gradually declines. It can be attributed to the cutting process in this cutting mode that begins with the maximum chip thickness, resulting in high-velocity impact stresses on the segments, as illustrated in Figure 12(a). In addition, since the rapid changes in impact and load during the cutting process, the substrate of the diamond circular saw blade is easily damaged, especially the segment or the bottom of the substrate water groove, which easily produces cracks and other problems. Consequently, a significant security risk is created in addition to shortening useful life of the circular saw blade. For this reason, the radius and structure of the water groove should be reasonably designed in engineering practice.

With the rotating tool linearly feeding, the stress is concentrated around the center hole of the tool and the impact zone of the segment with a maximum stress of 231 MPa, as shown in Figure 12(b). The crushing resistance of the spindle delivering power grows as the contact area between the saw blade and the rock increases, which then feeds back to the saw blade, resulting in stress concentration around the center hole. As the cutting process proceeds, the cutting kerf becomes longer and the restraint on the cutting tool is strengthened, which results in reduced transverse vibration of the saw blade and a lower stress value, as shown in Figures 12(c) and 12(d).

Clearly, the saw tooth segments in the arc region are subjected to alternating stress, and their von Mises stress changes accordingly. Excessive stress causes heat accumulation at the tool/workpiece contact zone, which aggravates tool wear and failure. Therefore, it is necessary to choose a reasonable cutting process and put forward higher criteria for saw blade material and segment structure. According to Figure 12, the von Mises stress of the saw blade varies from small to large throughout the cutting operation and then declines and stabilizes. It indicates that as the rock crushing area expands, the energy consumption of the disc cutter gradually decreases. At the same time, if the tool is subjected to excessive concentrated compressive stress during the cutting process, the saw blade is readily deformed, resulting in uneven stone saw roads, which not only generates severe vibration and noise but also aggravates wear and damage to the saw blade. As a result, before using the saw blade, it must be prestressed to compensate for the compressive stress created during the cutting operation.

4.4. Analysis of Cutting Force. The cutting forces of the circular saw blade are obtained through simulation and experimentation (Figure 13), and the cutting parameters are discussed in Section 3.1. The results with the average values of the vertical force and horizontal force at the stable stage in the experiments are 138.5 N and 201.0 N. The SPG numerical simulation results are 126.8 N and 180.3 N, and the FEM numerical simulation results are 159.3 N and 235.8 N, respectively, as shown in Figure 14. The numerical simulation

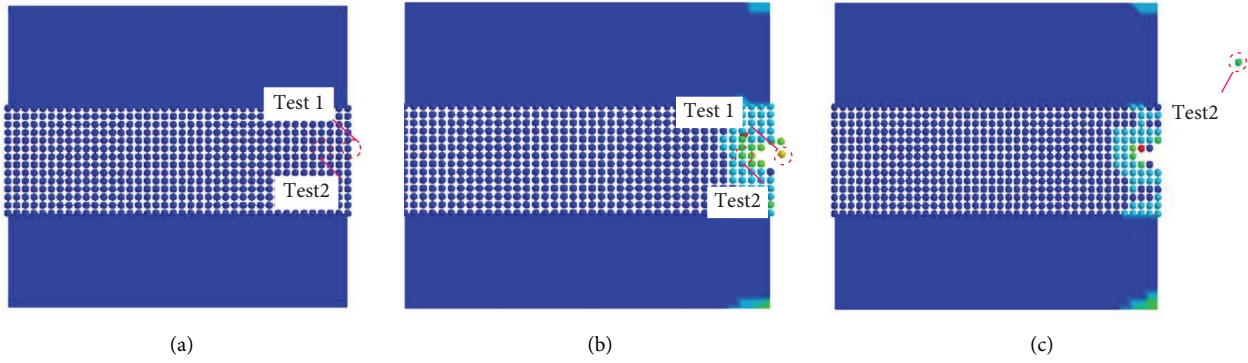


FIGURE 9: Testing points in different moment states: (a) initial state; (b) particle splash (test 1 point); (c) particle splash (test 2 point).

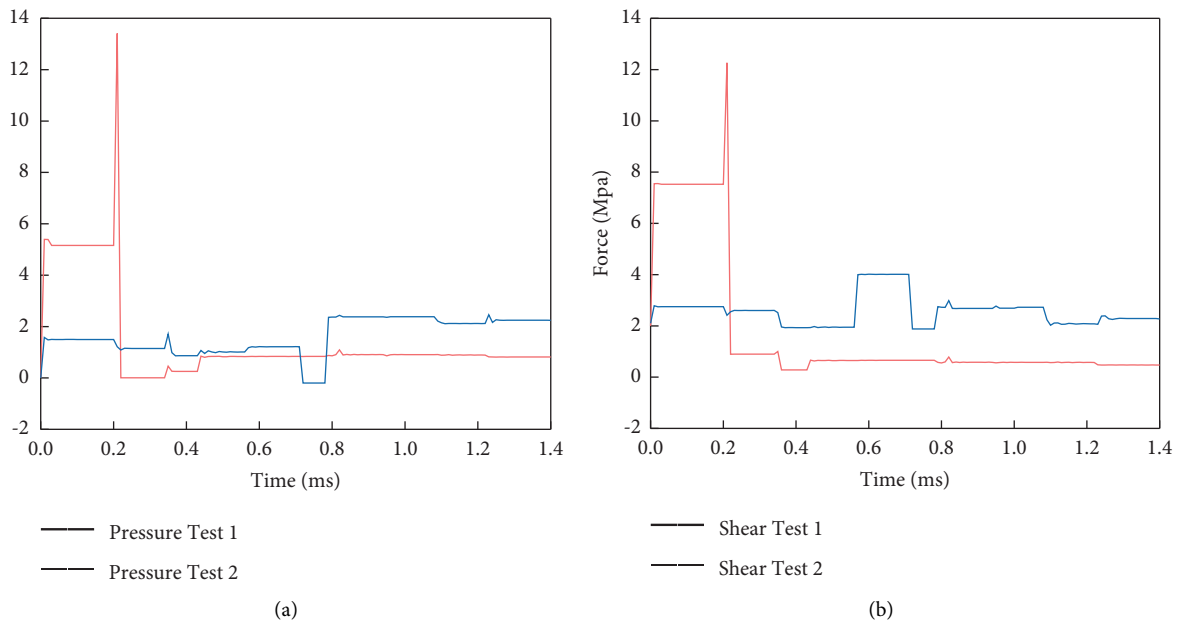


FIGURE 10: The variations in the stress and corresponding shear time: (a) pressure force; (b) shear force.

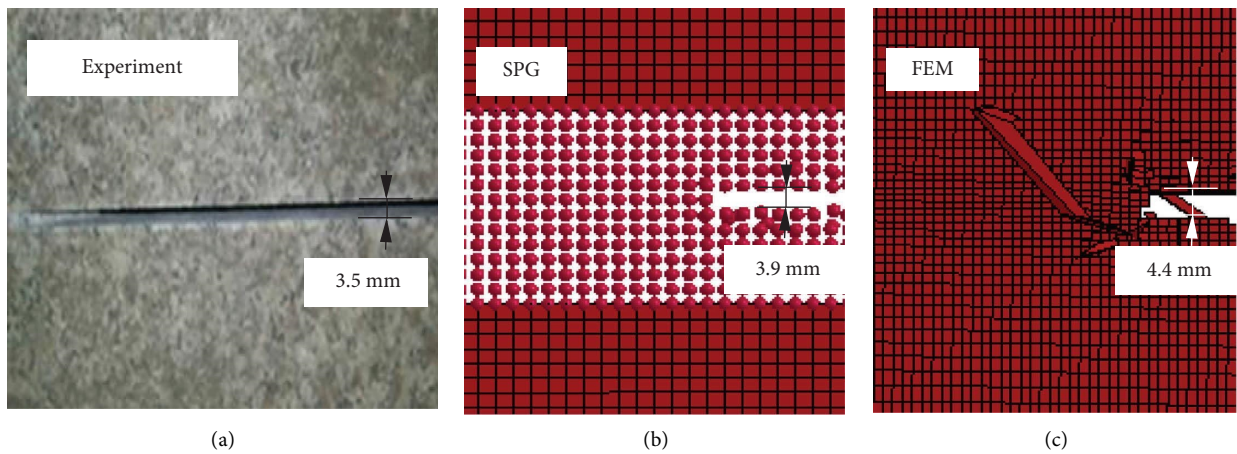


FIGURE 11: The width of saw kerf: (a) experimental result; (b) SPG simulation result; (c) FEM simulation result.

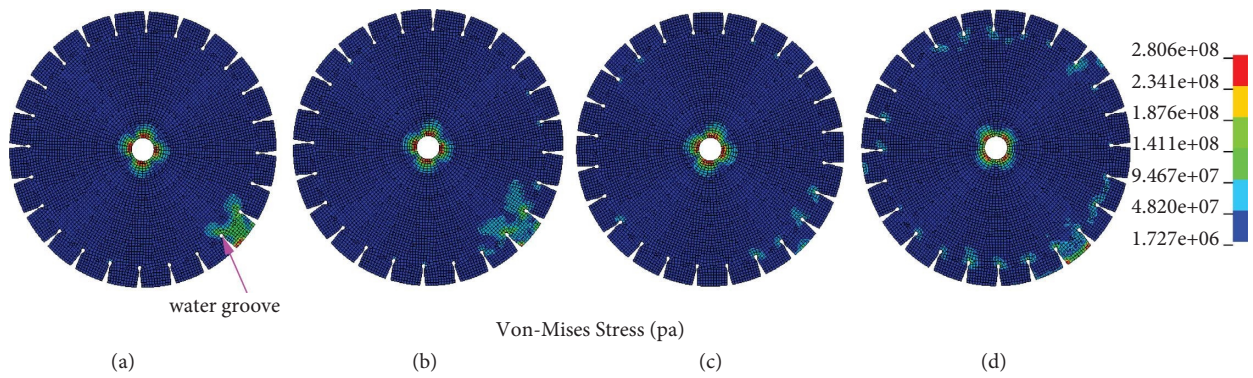


FIGURE 12: The von Mises stress nephogram at various cutting moments of circular saw blade: (a) 30th time step; (b) 200th time step; (c) 400th time step; (d) 600th time step.



FIGURE 13: The cutting force measurement system Kistler 9257B.

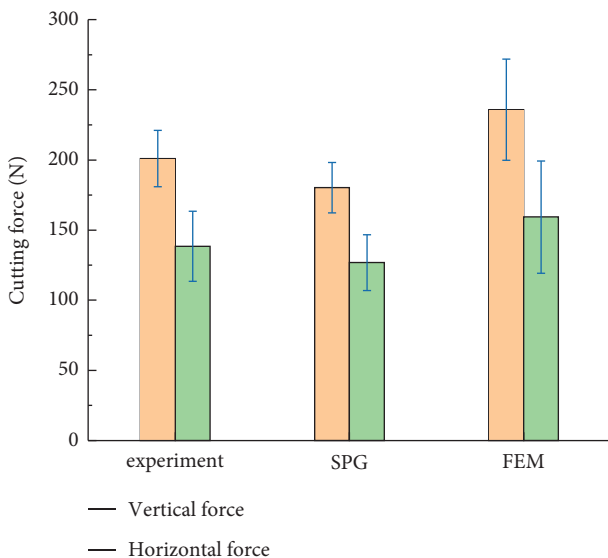


FIGURE 14: The cutting force of experimental results, SPG results, and FEM results.

did not account for stone hardness or cutting heat, resulting in lower SPG numerical simulation results than experimental values, with the tangential cutting force and normal cutting force being 8% and 10% smaller than the

experimental results, respectively. However, the experimental and numerical results of SPG remain consistent. The tangential and normal cutting forces in the FEM simulation, on the other hand, were 15% and 17% higher than the experimental values, respectively, and their fluctuations were large. As a result, the SPG model is superior to the FEM model in the simulating rock cutting system.

The cutting force F is a comprehensive force, which is the resistance of the tool against the workpiece material. It can not only describe the cutting mechanism and analyze the cutting quality of the stone but also directly determine the service life of the saw blade. As a result, this section investigates the cutting force under various cutting parameters.

When the tool makes contact with the workpiece, the impact action causes the cutting force to increase instantaneously. With the advancement in cutting movement, the cutting force shows a downward trend since the contact area between the saw blade and the rock reaches a threshold value and the saw kerf of the rock has a certain restriction on the saw blade. Subsequently, the cutting force fluctuates between 200 N and 240 N, indicating that the contact between the saw blade and the rock is discontinuous, nonlinear, and non-periodic and exhibits typical brittle material cutting characteristics, as illustrated in Figure 15(a). At various periods, the cutting force computed by the two methods is generally

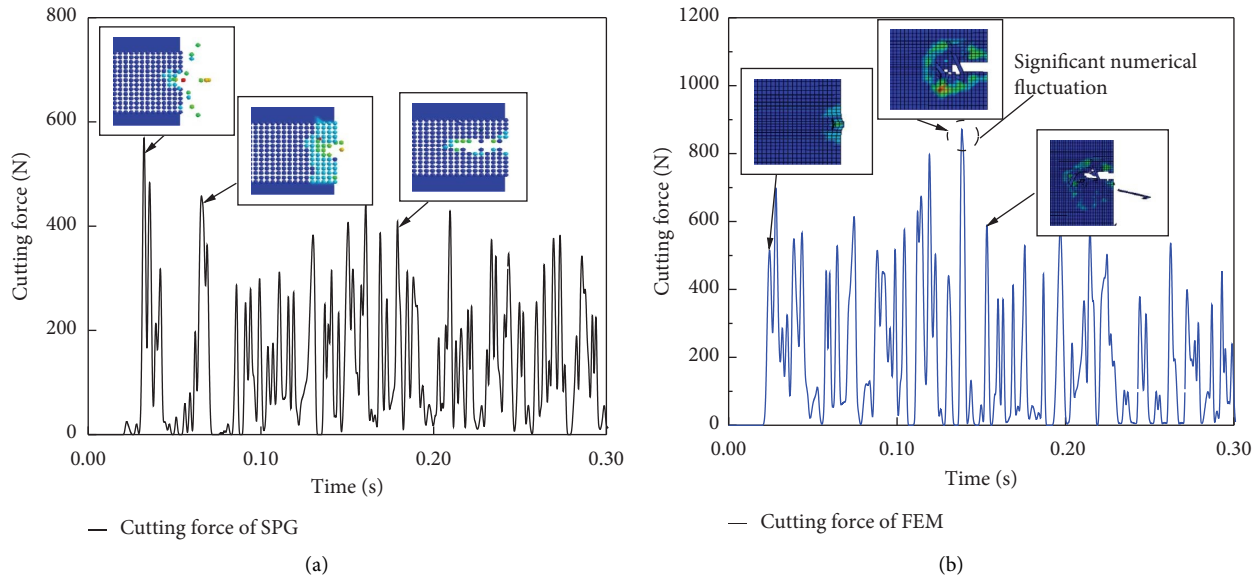


FIGURE 15: Time domain diagram of cutting force: (a) cutting force of SPG; (b) cutting force of FEM.

consistent. However, the numerical fluctuations of the cutting force are obvious at several points in the finite element algorithm calculation results. Because the mesh deforms after the rock element is stressed, when the mesh is deformed to a certain extent and removed under the failure condition, it causes abrupt changes in the cutting force, as illustrated in Figure 15(b). In addition, as the sudden failure of the element may lead to material vacancy, substantial mistakes will arise at certain moments. Therefore, the SPG model can more correctly describe rock cutting under high pressure and high-speed impact of the diamond saw blade.

Figure 16(a) depicts the cutting force curves when the circular cutting tool cut the rock at a rotation speed of 300 rad/s, a feed speed of 10 mm/s, and cutting depths of 7, 9, 11, and 13 mm. It is clear that increasing the cutting depth results in a large increase in cutting force. As the cutting depth increases, the overlapping area between the saw blade and the hard workpiece increases, and as the volume of stone removal per unit of time increases, the cutting force increases and converges to a stable value. In other words, with the increase in cutting depth, the number of rock fragments generated and acting on the interaction surface increases, leading to an increase in the cutting force. In addition, the same conclusions are available for different feed speeds of 0.12, 0.14, 0.16, and 0.20 mm/s. According to Figure 16(a), the relational expression between the cutting force and the cutting depth at different feed speeds was $y = Ax^2 + Bx + C$. It is apparent that these polynomial curves are fitted with high accuracy. In addition, the fluctuation of instantaneous cutting forces was more drastic at higher cutting depths and feed speeds, and when the cutting depth is 13 mm and the feed speed is 0.2 mm/s, the cutting force is 1280 N.

To investigate the relationship between saw blade feed speed and cutting force, the circular cutting tool was used to cut the rock with a rotation speed of 300 rad/s, a feed speed of 10 mm/s, and rotate speeds of 200, 240, 260, 280, and 300 rad/s, as shown in Figure 16(b). It is obvious that the

force increases with increasing feed speed. Such an increase of cutting forces has also been reported in FDEM simulation [24] and experimental analysis [25] for rock cutting. It could be attributed to the feed speed increasing and the volume of stone removal per unit time. To prevent saw blade wear and tear and extend tool life, the actual cutting operation should restrict the feed rate with the presumption that it would fulfill the requirements for cutting efficiency. Furthermore, when the cutting depth grows, the cutting force will be increased by comparing the force values. The relational expression between the cutting force and feed speed depth at different rotation speeds was $y = Ax^2 + Bx + C$. The correlation coefficient of different curves is presented in Figure 16(b). The fracture behavior and mechanical properties of the heterogeneous brittle rock are strain rate sensitive. The results of numerous studies have shown that the strength of rock materials increased as the strain rate increased [24]. It was believed that the enhancement of dynamic strength was primarily caused by the materials inhomogeneity and inertia effects. Because the rock material was assumed to be homogeneous and the material properties were constant in our simulation, the effect of cutting speed on cutting forces was mainly driven by inertia effects.

As shown in Figure 16(c), as the circular saw blade rotation speed increases, the cutting force reduces. The main reason for this is that as the rotation speed increases, the cutting force of the saw blade in contact with the rock increases relatively in the unit time, and thus the unit cutting force of each cutting-edge decreases resulting in the circular saw blade cutting force decreasing. Note that the removal volume of rock will be reduced by a circle of the cutting tool cutting rock with the rotation speed increasing, causing the discharge efficiency of rock fragments to increase and the cutting force to decrease. As a result, in engineering practice, increasing the rotation speed can be offered to reduce the cutting force. The relational expression between the cutting force and the rotation speed at different cutting depths was

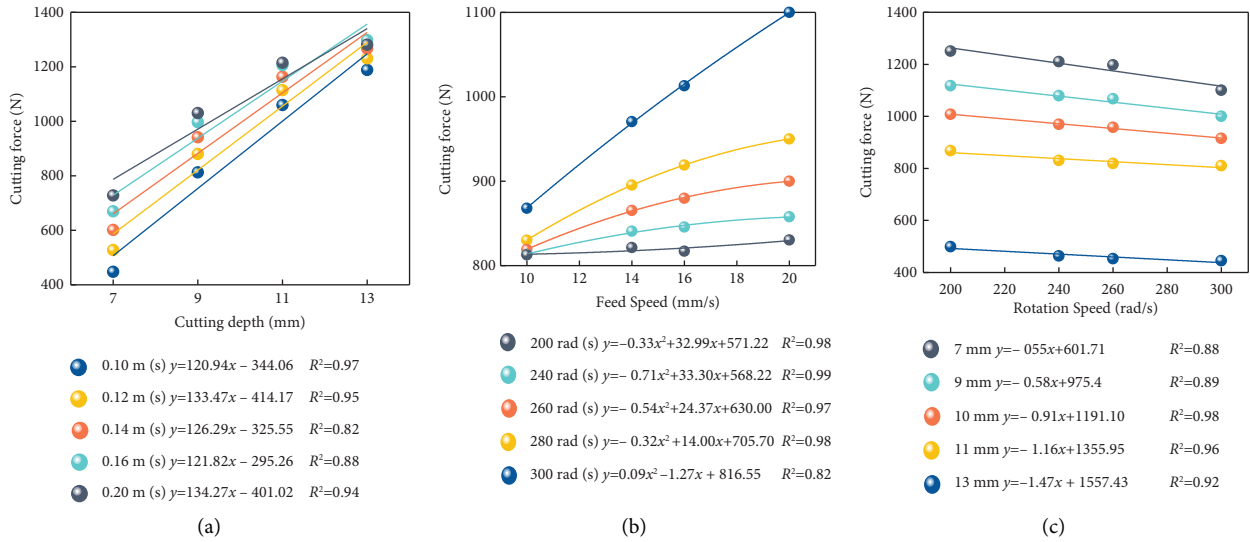


FIGURE 16: The relationship between cutting parameters and cutting forces: (a) relationship between the cutting force F and cutting depth with different feed speeds; (b) relationship between the cutting force F and feed speed with different rotation speeds; (c) relationship between the cutting force F and rotation speed with different cutting depths.

$y = Ax + B$. For instance, when the cutting depth is 0.13 mm, the parameters of the equation are $A = -1.47$ and $B = 1557.43$, and its correlation coefficient R is 0.97.

5. Conclusion

The process of cutting rock with the diamond circular saw blade is studied by the SPG simulation method in this paper. Four conclusions are drawn as follows:

- (1) The SPG approach can accurately characterize the processes by which hard and brittle materials are broken and destroyed, such as rock cutting with a circular saw blade. Meanwhile, the SPG method has low sensitivity to failure criteria when describing the damage of the rock, which makes the numerical robust and reliable since the major criteria for bond failure do not need to be tuned, which contrasts substantially with the element erosion type FEA. The simulation results are consistent with the experimental results for the time course of cutting force and saw blade vibration speed obtained by the SPG method. The accuracy of algorithm is demonstrated by the fact that the average values of sawing force and saw blade vibration speed from SPG numerical simulation do not exceed 11% of the experimental values.
- (2) During the cutting process, the saw blade segment is strongly squeezed and rubbed, resulting in saw blade wear primarily on the top and side of the saw tooth segment. Furthermore, the water groove of the circular saw blade is vulnerable to the damage from alternating stresses.
- (3) The damage to the rock in the cutting process is an intermittent and cyclic process separated into four stages: elastic deformation, local plastic deformation, small-scale extrusion, and large-scale fracture.

- (4) There is a significant correlation between cutting force and cutting parameters. The cutting force increases with the increase in the cutting depth and feed speed and decreases with the increase in the rotation speed. Within the range of the proposed test parameters, priority parameters can be given in engineering practice to reduce cutting depth, increasing rotation speed, and decreasing feeding rate to minimize the cutting force.

The economic cost can be reduced by simulating and analyzing the rock cutting process. In the simulation analysis, the microscopic mechanism of the rock cutting process by diamond saw blade can be further analyzed, and it can also perform the thermodynamic coupling analysis of the cutting process.

Data Availability

The data used to support the findings of this study are included within the article.

Conflicts of Interest

The authors declare that there are no conflicts of interest regarding the publishing of this paper.

Acknowledgments

This work was supported by the projects of the Tianjin Municipal Education Commission Scientific Research Project of China (Grant no. 2021KJ022), the National Vocational Education Teacher and Teaching Innovation Team Project Construction of China (Grant no. ZH2021020201), and the Scientific Research Foundation of Tianjin University of Technology and Education (Grant no. KYQD202202).

References

- [1] J. Zhou, K. Wang, J. Zhang, H. Zhang, T. Cao, and J. Ju, "Rock breakage and tools performance during rock processing by multidiameter combination saw with different diameters," *Rock Mechanics and Rock Engineering*, vol. 55, pp. 4459–4476, 2022.
- [2] Z. Wang, Q. Zeng, Z. Lu, Z. Liu, and X. Li, "Numerical investigation of the rock cutting performance of a circular sawblade," *Mathematical Problems in Engineering*, vol. 2020, Article ID 9706183, 18 pages, 2020.
- [3] S. Wen and C. Zhang, "Experimental and simulation study on rock-breaking efficiency of disc cutters on composite rocks," *International Journal of Rock Mechanics and Mining Sciences*, vol. 153, Article ID 105089, 2022.
- [4] Z. Lu, Q. Zeng, Z. Wang, X. Li, and K. Gao, "Experimental and numerical studies on rock cutting with saw blade and conical pick combined cutting method," *Mathematical Problems in Engineering*, vol. 2019, Article ID 5046873, 14 pages, 2019.
- [5] Y. Wicaksana, H. Jeong, and S. Jeon, "Numerical simulation of rock cutting process induced by a pick cutter considering dynamic properties of rock at intermediate strain rate," *Bulletin of Engineering Geology and the Environment*, vol. 80, no. 12, pp. 9049–9069, 2021.
- [6] Z. Zhang, K. Zhang, W. Dong, and B. Zhang, "Study of rock-cutting process by disc cutters in mixed ground based on three-dimensional particle flow model," *Rock Mechanics and Rock Engineering*, vol. 53, no. 8, pp. 3485–3506, 2020.
- [7] M. Gao, K. Zhang, Q. Zhou, H. Zhou, B. Liu, and G. Zheng, "Numerical investigations on the effect of ultra-high cutting speed on the cutting heat and rock-breaking performance of a single cutter," *Journal of Petroleum Science and Engineering*, vol. 190, Article ID 107120, 2020.
- [8] H. Jiang, H. Zhao, K. Gao, O. Wang, Y. Wang, and D. Meng, "Numerical investigation of hard rock breakage by high-pressure water jet assisted indenter impact using the coupled SPH/FEM method," *Powder Technology*, vol. 376, pp. 176–186, 2020.
- [9] M. Hillman, J. S. Chen, and S. W. Chi, "Stabilized and variationally consistent nodal integration for meshfree modeling of impact problems," *Computational Particle Mechanics*, vol. 1, no. 3, pp. 245–256, 2014.
- [10] H. Jeong, S. Choi, S. Lee, and S. Jeon, "Rock cutting simulation of point attack picks using the smooth particle hydrodynamics technique and the cumulative damage model," *Applied Sciences*, vol. 10, no. 15, p. 5314, 2020.
- [11] A. Mardalizad, T. Saksala, A. Manes, and M. Giglio, "Numerical modeling of the tool-rock penetration process using FEM coupled with SPH technique," *Journal of Petroleum Science and Engineering*, vol. 189, Article ID 107008, 2020.
- [12] J. S. Chen, C. T. Wu, S. Yoon, and Y. You, "A stabilized conforming nodal integration for Galerkin meshfree methods," *International Journal for Numerical Methods in Engineering*, vol. 50, no. 2, pp. 435–466, 2001.
- [13] C. T. Wu, Y. Wu, D. Lyu, X. Pan, and W. Hu, "The momentum-consistent smoothed particle Galerkin (MC-SPG) method for simulating the extreme thread forming in the flow drill screw-driving process," *Computational Particle Mechanics*, vol. 7, no. 2, pp. 177–191, 2020.
- [14] J. S. Chen, M. Hillman, and M. Rüter, "An arbitrary order variationally consistent integration for Galerkin meshfree methods," *International Journal for Numerical Methods in Engineering*, vol. 95, no. 5, pp. 387–418, 2013.
- [15] P. Guan, J. Chen, Y. Wu et al., "Semi-Lagrangian reproducing kernel formulation and application to modeling earth moving operations," *Mechanics of Materials*, vol. 41, no. 6, pp. 670–683, 2009.
- [16] S. W. Chi, C. H. Lee, J. S. Chen, and P. C. Guan, "A level set enhanced natural kernel contact algorithm for impact and penetration modeling," *International Journal for Numerical Methods in Engineering*, vol. 102, no. 3-4, pp. 839–866, 2014.
- [17] C. T. Wu, M. Koishi, and W. Hu, "A displacement smoothing induced strain gradient stabilization for the meshfree Galerkin nodal integration method," *Computational Mechanics*, vol. 56, no. 1, pp. 19–37, 2015.
- [18] Y. Wu and C. T. Wu, "Simulation of impact penetration and perforation of metal targets using the smoothed particle Galerkin method," *Journal of Engineering Mechanics*, vol. 144, no. 8, Article ID 04018057, 2018.
- [19] Y. Zhang, F. An, S. Liao, C. Wu, J. Liu, and Y. Li, "Study on numerical simulation methods for hypervelocity impact on large-scale complex spacecraft structures," *Aerospace*, vol. 9, no. 1, p. 12, 2021.
- [20] A. Mardalizad, R. Scazzosi, A. Manes, and M. Giglio, "Testing and numerical simulation of a medium strength rock material under unconfined compression loading," *Journal of Rock Mechanics and Geotechnical Engineering*, vol. 10, no. 2, pp. 197–211, 2018.
- [21] A. Mardalizad, M. Caruso, A. Manes, and M. Giglio, "Investigation of mechanical behaviour of a quasi-brittle material using Karagozian and Case concrete (KCC) model," *Journal of Rock Mechanics and Geotechnical Engineering*, vol. 11, no. 6, pp. 1119–1137, 2019.
- [22] A. Mardalizad, A. Manes, and M. Giglio, "The numerical modelling of a middle strength rock material under Flexural test by Finite Element method-coupled to-SPH," *Procedia Structural Integrity*, vol. 3, pp. 395–401, 2017.
- [23] R. P. Bohara, G. Tanapornraweeakit, and S. Tangtermsirikul, "Investigation of concrete material models for analysis of seismic behavior of reinforced concrete under reversed cyclic load," *Songklanakarin Journal of Science and Technology*, vol. 41, no. 4, pp. 951–958, 2019.
- [24] F. Z. Wang, S. Y. Liu, and K. X. Ji, "Numerical study on abrasive machining of rock using FDEM method," *Simulation Modelling Practice and Theory*, vol. 104, Article ID 102145, 2020.
- [25] F. Z. Wang, S. Y. Liu, Z. Y. Guo, and L. Cao, "Analysis of cutting forces and chip formation in milling of marble," *International Journal of Advanced Manufacturing Technology*, vol. 108, no. 9-10, pp. 2907–2916, 2020.